J. Fluid Mech. (1989), *vol.* 208, *pp.* 1–23
Printed in Great Britain

Origin of the peak–valley wave structure leading to wall turbulence

By MASAHITO ASAI AND MICHIO NISHIOKA
Department of Aeronautical Engineering, University of Osaka Prefecture,
Sakai, Osaka 591, Japan

(Received 4 January 1988 and in revised form 13 January 1989)

A generation process for the three-dimensional wave which dominates the transition preceded by a Tollmien–Schlichting (T–S) wave is studied both experimentally and numerically in plane Poiseuille flow at a subcritical Reynolds number of 5000. In order to identify the origin of the three-dimensional wave in Nishioka *et al.*'s laboratory experiment, the corresponding spanwise mean-flow distortion and two-dimensional T–S wave modes are introduced into a parabolic flow as the initial disturbance conditions for a numerical simulation of temporally growing type. Through reproducing the actual wave development into the peak–valley structure, the simulation pinpoints the origin to be the slight spanwise mean-flow distortion in the experimental basic flow. Furthermore, the simulation clearly shows that the growth of the three-dimensional wave requires the vortex stretching effect due to the streamwise vortices, which appear under the experimental conditions only when the amplitude of the two-dimensional T–S wave is above the observed threshold.

1. Introduction

Since a series of elaborate experiments on the ribbon-induced transition in Blasius flow by Klebanoff & Tidstrom (1959), Klebanoff, Tidstrom & Sargent (1962), Kovasznay, Komoda & Vasudeva (1962) and Hama & Nutant (1963), the three-dimensional wave development of an initially two-dimensional wave has been well-recognized. Indeed, the prerequisite for the eventual breakdown into turbulence is the occurrence and growth of three-dimensionality leading to a spanwise-periodic wave motion, i.e. the so-called peak–valley structure. It is, however, only recently that we have gradually obtained a better understanding of the mechanism for the three-dimensional wave development, as reviewed by Tani (1981), Morkovin (1983), Herbert (1984*a*), Craik (1985) and Stuart (1986).

With respect to theoretical developments, Benney & Lin (1960) modelled the so-called longitudinal vortices associated with the peak–valley structure (that cause the local high-shear layers to form at spanwise peak positions as demonstrated by Stuart 1965) through considering the second-order effects of the interaction between the primary two-dimensional Tollmien–Schlichting (T–S) wave and a pair of oblique waves (of the same streamwise wavenumber) with the spanwise periodicity: Klebanoff *et al.* (1962) supported this model of the formation of the longitudinal vortices. A more rational analysis of this kind of interaction was made by Stuart (1962) on the basis of weakly nonlinear theory. Craik (1971) proposed a resonant wave triad: a resonance between the fundamental two-dimensional wave and a pair of subharmonic oblique waves. Kachanov & Levchenko (1984) observed Craik's mechanism to operate in experiments, depending on the disturbance environment.

Saric & Thomas (1984) visualized two types of subharmonic modes, each of which developed into a staggered peak–valley structure quite different from the Klebanoff-type ordered peak–valley: one was interpreted as a result of Craik's mechanism and the other was explained by using Herbert's secondary instability model (described below).

In plane Poiseuille flow, continued experimental, theoretical and numerical efforts of many authors have also significantly contributed to the progress in understanding the fundamental problem of the transition initially controlled by T–S waves. Nishioka, Iida & Ichikawa (1975), Nishioka, Iida & Kanbayashi (1978), Nishioka, Asai & Iida (1980, 1981), Nishioka & Asai (1984, 1985*a*, *b*) have been studying the ribbon-induced transition at sub- and super-critical Reynolds numbers to clarify the linear instability (1975), the nonlinear subcritical instability (put forward by Stuart 1960) (1975, 1985*a*), the peak–valley development (1978, 1980, 1985*b*), the high-frequency instability (of the high-shear layer) into hairpin eddies (1980, 1981), and the final evolution into wall-turbulence (1981, 1984). Because the nature of three-dimensional wave growth is found to be almost independent of the Reynolds number R (defined on the channel half-depth h and the centreline velocity U_c), the experiments have been done mainly at $R = 5000$ and at a ribbon frequency $f = 72$ Hz ($2\pi fh/U_c = 0.337$). In spite of the subcritical Reynolds number ($R = 5000$, 86% of the critical R for linear instability), it is shown that the excited wave can grow when the initial amplitude exceeds a threshold, about $0.01U_c$ in r.m.s. terms. As the wave grows, the initial slight spanwise distortion of the wave front is intensified to develop into the ordered peak–valley structure. In the beginning, the intensification proceeds near the critical layer only. No large distortion occurs near the centreline until the high-shear layer breaks down into hairpin eddies. The observed threshold behaviour of the initial wave growth is in reasonable agreement with the prediction from weakly nonlinear theory for two-dimensional T–S waves: for the two-dimensional threshold, see Itoh (1974), Herbert (1977) and Fasel & Bestek (1980), and for the threshold behaviour of oblique waves, see Dhanak (1983). Moreover, the observed amplification of the initial three-dimensionality clearly indicates that the almost streamwise-periodic flow near the subcritical equilibrium is highly sensitive to three-dimensional disturbances.

Therefore, on the basis of Stuart's (1962) weakly nonlinear theory including three-dimensional disturbances, Itoh (1980) studied three-dimensional effects and found similar threshold behaviour in plane Poiseuille flow, though the parameter range in his calculation was different from ours. Subsequently, Kleiser (1982) succeeded in reproducing our laboratory experiment (at least up to the stage of the formation of high-shear layer) through a numerical simulation of temporally growing type and demonstrated the threshold behaviour in the growth of the initially imposed small-amplitude three-dimensional wave disturbances (i.e. a pair of oblique Orr–Sommerfeld modes). Orszag & Patera (1983) also showed a similar three-dimensional development numerically.

These experimental and numerical results encouraged Orszag & Patera (1983) and Herbert (1984*a*, *b*) to model the three-dimensional wave growth as a linear secondary instability of the basic flow modified by a finite-amplitude T–S wave with respect to three-dimensional disturbances. Solving the eigenvalue problem for the case of our experiment, Herbert found two different three-dimensional modes, i.e. those with fundamental and subharmonic frequencies, and interpreted that they are respectively responsible for the ordered peak–valley observed by Nishioka *et al.* and the staggered peak–valley visualized by Kozlov & Ramazanov (1983). To clarify the

instability, it is necessary to identify the structure of the instability wave. So, through a painstaking double Fourier analysis (of the u-velocity fluctuation) with respect to the frequency and the spanwise wavenumber, Nishioka & Asai (1985*b*) have tried to identify the three-dimensional modes actually dominating the ordered peak–valley development, and have shown that Herbert's model well describes the actual three-dimensional wave motions. Singer, Reed & Ferziger (1986) used a 'random noise' as the initial three-dimensional disturbances to make a numerical simulation not unlike Kleiser's. The 'random' component in Singer *et al.*'s initial conditions was introduced by adding a small random number to each velocity component at every grid point. In the simulation of temporally growing type, it is worth noting that according to DiPrima & Habetler (1969), such initial disturbances may be decomposed into oblique Orr–Sommerfeld (and/or Squire) modes and are thus different from the actual random noise, including sound noise and free-stream turbulence. The results of their simulation show that both fundamental and subharmonic three-dimensional modes can develop depending on the magnitude of the two-dimensional T–S wave just as predicted by Herbert's model. Singer *et al.* also observed that longitudinal vortices added to the above-mentioned initial field can suppress the subharmonic mode, while accelerating the growth of the fundamental mode.

In spite of these experimental and numerical efforts, which definitely support Herbert's secondary instability model, a crucial question is left open concerning the effect of mean-flow distortion on the generation of three-dimensional wave disturbances. The question is really important as it is related to the origin of the three-dimensional waves dominating the transition under consideration. As will be briefly described in §2, our basic flow has an almost periodic spanwise variation (of the order of 2% in U_c at most) which determines the spanwise positions of peak–valley structure, so that the flow condition is not the same as Herbert's model which assumes no spanwise distortion in the basic flow. On the other hand, the residual turbulence is quite low, being less than 0.05% of U_c and mainly consisting of low-frequency components. These facts suggest a high possibility that the two-dimensional T–S wave interacts with the three-dimensional (spanwise periodic) steady distortion to generate three-dimensional wave disturbances, which then resonate with the two-dimensional wave and develop into three-dimensional wave modes not unlike the eigenmode predicted by Herbert's model above the threshold. Herbert's secondary instability model does not provide any information on the source (or origin) of the three-dimensional waves actually excited in a particular flow condition. Although Herbert & Morkovin (1980) and Itoh (1987) pointed out the importance of this kind of interaction, they could not make clear the occurrence and growth process of the three-dimensional wave modes observed. This is also the case in Singer *et al.* (1986, 1987) who used longitudinal vortices and oblique waves as a part of the initial conditions as mentioned earlier. So the present authors decided to examine and follow up the possible generation and growth of the three-dimensional wave modes from the interaction between the three-dimensional steady distortion and the two-dimensional T–S wave, through a numerical simulation.

In our laboratory experiment, the slight spanwise periodic distortion in the basic flow is probably due to some inevitable non-uniformities of the damping screens (in particular, the farthest downstream one) and/or the wall curvature of the contraction section where Görtler-type vortices may appear. Whatever the causes are, there is little doubt that at subcritical Reynolds numbers the possible mean flow distortion at the channel inlet decays downstream, and nothing more happens if it is initially

weak, without accompanying strong residual turbulence. Therefore, it may be expected that in the test section (beyond $600h$ from the channel inlet), the possible small remnant of the inlet flow distortion is expressed in terms of the eigenmodes (for spanwise mean-flow distortion) derived from the linear stability equations for the distortion of ideally two-dimensional parabolic flow. This will be clarified in §3. For the numerical simulation in §4, we shall select one of the three-dimensional eigenmodes which has no cross-stream velocity components and best approximates the actual spanwise periodic distortion in our experimental basic flow (at $R = 5000$).

2. Initial three-dimensionality eventually dominating the transition

Using a long rectangular wind tunnel of large aspect ratio (27.4), we have been studying the ribbon-induced transition in plane Poiseuille flow mainly at a subcritical Reynolds number $R = 5000$ ($U_c = 9.8$ m/s, $h = 7.3$ mm). Detailed experimental procedures are described in Nishioka & Asai (1985*b*). Here we shall describe briefly the three-dimensional features of the initial wave development observed with a hot-wire at an x-station $48h$ downstream of the ribbon vibrating at

$$f = 72 \text{ Hz } (2\pi fh/U_c = 0.337).$$

To illustrate the three-dimensionality of the basic flow, figure 1 shows the spanwise (z) distributions of the local velocity U at various y-positions in the lower half of the channel at $R = 5000$; *the* y-axis (normal to wall) is measured from the channel centre. The figure compares three sets of data measured in different years to show that there are slight but non-negligible differences in the magnitude and detailed pattern of the three-dimensionality. No doubt, this is because the wind-tunnel conditions (for instance, inevitable dust accumulation on the damping screens in the settling chamber) were not exactly the same. Importantly, however, the global patterns are similar to each other (and well represented by solid lines as discussed later), so the reproducibility of the experiment has been maintained. The spanwise variations of local U are almost periodic with a dominant wavelength of about 25 mm ($= 3.4h$) near the centreline; the three-dimensionality of the basic flow will be examined in detail in §3. As already noted in our previous papers (Nishioka *et al.* 1978, 1980; Nishioka & Asai 1985*b*), the excited wave is affected by the three-dimensionality in the basic flow, even when the excitation is weak and the wave amplitude is below the threshold for the onset of the peak–valley splitting. Figure 2(*a*) illustrates this feature for a wave with u'_m (maximum r.m.s. amplitude) = 0.35% of U_c. Indeed, the three-dimensional plotting of the u-fluctuation indicates that the excited wave is not purely two-dimensional but exhibits a slight spanwise distortion; time t runs backwards so as to provide a near-simulation of the wave coming out of the paper. The three-dimensionality is shown more quantitatively in figures 2(*b*) and 2(*c*), where the r.m.s. intensity of the u-fluctuation, u', at $y/h = -0.815$ and the phase of the fundamental frequency (72 Hz) component θ at $y/h = -0.73$ are respectively plotted against z. It may be seen that the spanwise phase distribution is almost periodic with a dominant wavelength (about $3.4h$) imposed by the corresponding variation in the centreline velocity, though the three-dimensionality is quite small as seen in the amplitude distribution, and the wave is ascertained to be of two-dimensional T–S type (the wavelength λ_{TS} is $5.4h$). As the amplitude of this primary wave is increased this initial three-dimensionality becomes amplified as shown in figure 3 (also presented in Nishioka & Asai 1985*b*) and leads to the peak–valley development, which is well-controlled in the sense that the peak–valley positions are

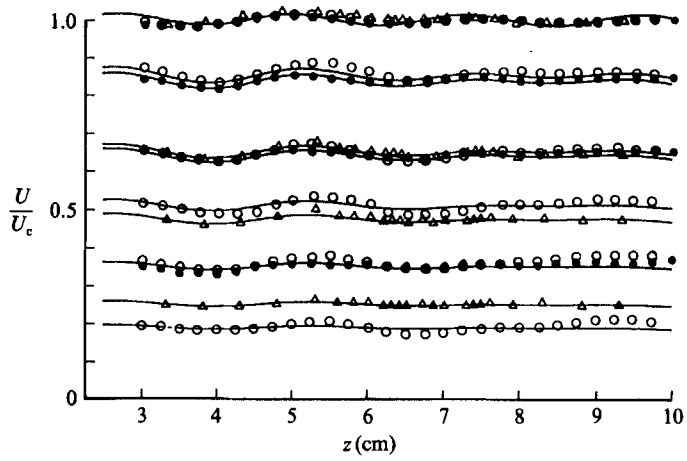

FIGURE 1. Spanwise distortion of the basic flow at $R = 5000$: △, Nishioka *et al.* (1978); ○, Nishioka & Asai (1985*b*); ●, present. Solid lines represent equation (9): y/h (from top) = 0, −0.39, −0.41, −0.59, −0.60, −0.70, −0.73, −0.80, −0.86, −0.90.

fixed and the total wave system is periodic in time: u'_m (shown as 1.8% and 3.0% in the figure) denotes the y-maximum of the r.m.s. value u' at a spanwise peak position, $z = 7.5$ cm. Here it is worth noting that in both halves of the channel ($y \gtrless 0$), the spanwise peaks appear at the same z-positions, i.e. at the z-positions where U_c takes local maxima.

Figure 4 also shows the three-dimensionality of the wave motion at various stages by plotting the z-distributions of u' at $y/h = -0.815$. The detail of the observed peak–valley wave development depends on the three-dimensionality in the basic flow, as demonstrated by two sets of data which were obtained in Nishioka & Asai (1985*b*) and the present study. It is interesting to note that in spite of rather clear difference in the degree of the three-dimensionality in the basic flow (as seen in figure 1), we see almost no difference in the two sets of data for u' in figure 4, except that the spanwise distributions are more periodic in the present experiment, just like the corresponding basic flow. This means that even the slightest three-dimensionality of the present basic flow has decisive effects on the peak–valley wave development.

The well-controlled, periodic feature enables us to decompose the fluctuation field into two- and three-dimensional wave components by means of a double Fourier analysis with respect to the frequency and the spanwise wavenumber. Indeed, Nishioka & Asai (1985*b*) have performed the analyses for the u-fluctuation field at the $u'_m/U_c = 1.8\%$ and 5.5% stages, where the peak–valley wave motion is fully established, and have observed that the two-dimensional wave is exactly the T–S mode and the three-dimensional wave thus singled out is well represented by the three-dimensional eigenmode of Herbert's model. But Nishioka & Asai (1985*b*) have not performed the analyses below and around the threshold. So, as the first step of the present study, we have done a double Fourier decomposition for the smaller-amplitudes cases in order to clarify the threshold behaviour of the three-dimensional mode. The three-dimensional wave mode (of fundamental frequency f and dominant spanwise wavenumber $\beta_* = 2\pi/3.4h$), which as shown in Nishioka & Asai (1985*b*) consists of a pair of right- and left-moving oblique waves of almost equal amplitude, is written as follows at a fixed x-position:

$$u_{3D} = \hat{u}_{3D}(y)\cos(2\pi ft + \theta_{3D}(y))\cos(\beta_*(z - z_p)), \tag{1}$$

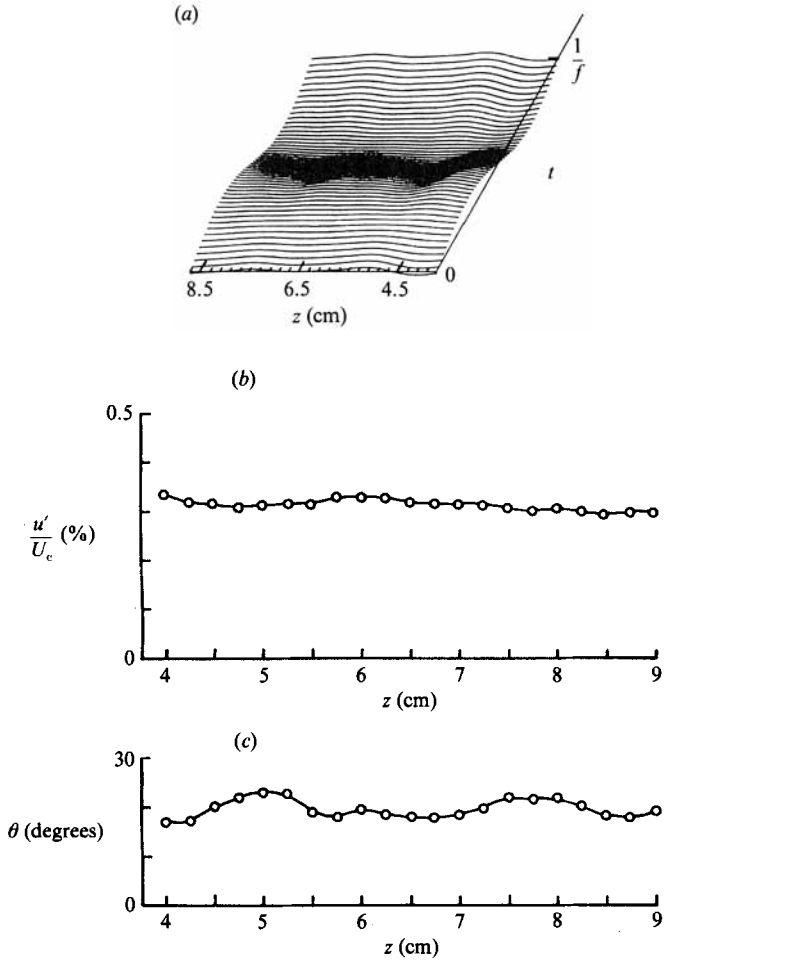

FIGURE 2. Initial three-dimensionality of the excited wave (72 Hz) at $R = 5000$. (*a*) Three-dimensional plot of the u-fluctuation at $y/h = -0.8$; (*b*) r.m.s. amplitude u'/U_c at $y/h = -0.815$; (*c*) phase θ at $y/h = -0.73$.

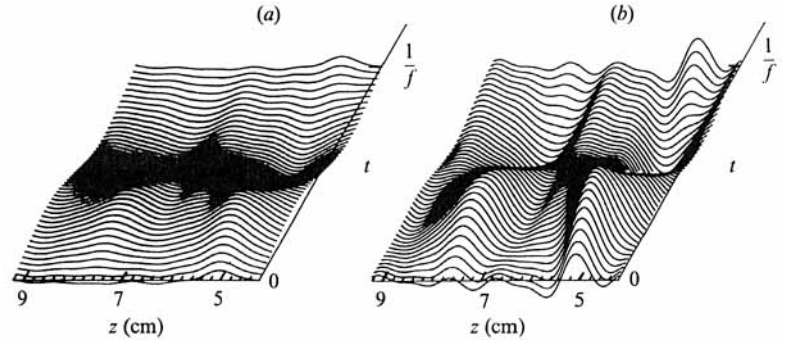

FIGURE 3. Three-dimensional wave growth leading to peak–valley structure, illustrated by means of the u-fluctuation at $y/h = -0.815$. (*a*) $u'_m/U_c = 1.8\%$; (*b*) $u'_m/U_c = 3.0\%$.

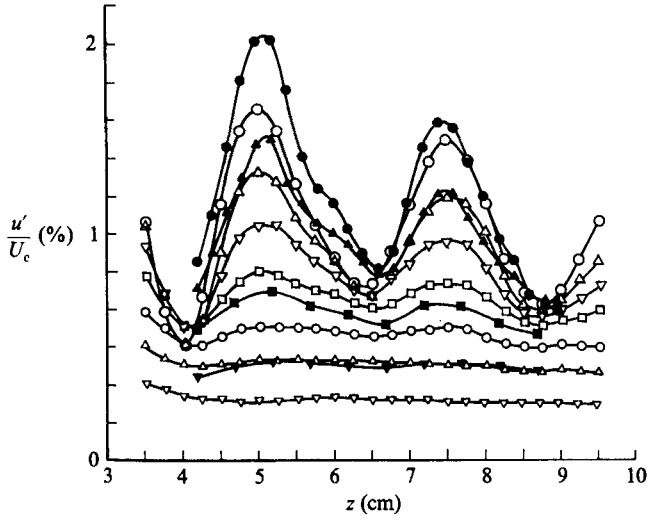

FIGURE 4. z-distributions of u' at $y/h = -0.815$, at various stages. ● ▲ ▼ ■, Nishioka & Asai (1985*b*); ○ △ ▽ □, present.

where z_p denotes the spanwise peak. We shall use this equation to define the amplitude $\hat{u}_{3D}$ and the phase θ_{3D} for the three-dimensional wave mode. The y-maximum of $\hat{u}_{3D}$ is denoted as A_{3max}, and similarly the y-maximum of the two-dimensional T–S wave as A_{2max} for the following discussion.

To examine the relationship between the two-dimensional T–S wave and the three-dimensional wave mode (of dominant spanwise wavelength $3.4h$), figure 5(*a*) plots A_{3max} versus A_{2max}: the measurements are made at a fixed x-station ($48h$ downstream from the ribbon) by varying the ribbon amplitude, and double Fourier analyses are carried out on the data to obtain A_{2max} and A_{3max}. From the figure we see that when the amplitude of the two-dimensional T–S mode A_{2max} is less than 1.0% of U_c, the amplitude of the three-dimensional mode A_{3max} is linearly proportional to A_{2max}. However, as A_{2max} is increased beyond that level by increasing the ribbon amplitude, the ratio A_{3max}/A_{2max} ceases to remain constant and starts to grow. The growth of A_{3max} (relative to A_{2max}) becomes pronounced beyond $A_{2max}/U_c = 1.4\%$ (or 1% in terms of the r.m.s. value), which is the value often cited as the threshold for the peak–valley splitting following Nishioka *et al.* (1978, 1980). Figure 5(*b*) shows the phase difference between the two-dimensional T–S and three-dimensional modes $(\theta_{3D} - \theta_{2D})$ at $y/h = -0.815$. In the case of weak excitation where A_{3max}/A_{2max} remains constant, the phase difference also remains almost constant. However, it starts to change at about $A_{2max}/U_c = 1.0\%$ and approaches another constant (represented by a broken line) as A_{2max}/U_c exceeds about 1.4%. The broken line is from the prediction of Herbert's secondary instability model (for the case of the subcritical two-dimensional equilibrium at $R = 5000$ and $2\pi h/\lambda_{TS} = 1.12$, i.e. $A_{2max}/U_c = 3.0\%$). It should be also noted that the phase difference between the two-dimensional mode and the ribbon current signal remains constant at each y-position over the whole range of excitation shown here. These results suggest that only the three-dimensional wave changes its structure and behaviour at and around $A_{2max}/U_c = 1\%$. It has already been shown by Nishioka & Asai (1985*b*) that the three-dimensional mode at $u'_m/U_c = 1.8\%$ ($A_{2max}/U_c = 2.0\%$) has almost the same

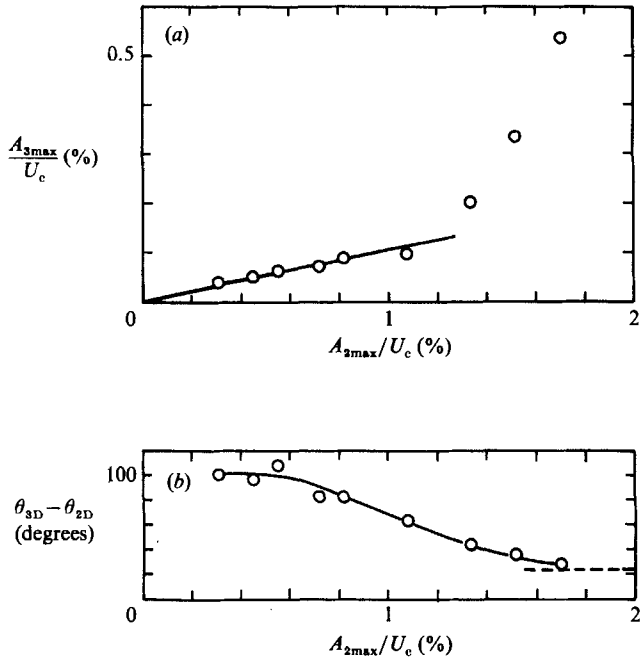

FIGURE 5. Threshold behaviour of the three-dimensional wave mode. (*a*) A_{3max} *vs.* A_{2max}; (*b*) $\theta_{3D}-\theta_{2D}$ *vs.* A_{2max}. The broken line in (*b*) is from the prediction of Herbert's secondary instability model.

structure as that of the eigenmode of the secondary instability model: the three-dimensional wave mode for the case of weak excitation (i.e. $A_{2max}/U_c < 1.0\,\%$) will be described later.

3. Theoretical considerations of the three-dimensionality of the experimental basic flow

From the experimental results described thus far, we have learned that in its structure and behaviour the three-dimensional wave under consideration is highly dependent on both the two-dimensional T–S wave and the initial three-dimensionality in the basic flow. This means that it is quite important to identify the three-dimensionality in our basic flow in as much detail as possible. Because the three-dimensionality is less than 2.5 % of U_c in magnitude, it is highly probable that such a small distortion can be described by linear stability theory. For simplicity, we consider the temporally growing case, where the distortion mode $\boldsymbol{v}_0(y,z,t) = (u_0, v_0, w_0)$ takes the form

$$\boldsymbol{v}_0 = \begin{pmatrix} \hat{u}_0(y)\cos(\beta z) \\ \hat{v}_0(y)\cos(\beta z) \\ \hat{w}_0(y)\sin(\beta z) \end{pmatrix} \mathrm{e}^{\gamma t}, \tag{2}$$

and $(\hat{u}_0(y), \hat{v}_0(y), \hat{w}_0(y))$ is calculated from the following linearized equations written in non-dimensional form (scaled with the channel half-depth h and centreline velocity U_c):

$$\left(\frac{\mathrm{d}^2}{\mathrm{d}y^2}-\beta^2\right)\left(\frac{\mathrm{d}^2}{\mathrm{d}y^2}-\beta^2-\gamma R\right)\hat{v}_0 = 0, \tag{3}$$

$$\left(\frac{\mathrm{d}^2}{\mathrm{d}y^2}-\beta^2-\gamma R\right)\hat{u}_0 = R\frac{\mathrm{d}U}{\mathrm{d}y}\hat{v}_0, \tag{4}$$

$$\frac{\mathrm{d}\hat{v}_0}{\mathrm{d}y}+\beta\hat{w}_0 = 0, \tag{5}$$

$$\hat{u}_0 = \hat{v}_0 = \hat{w}_0 = 0 \quad \text{at} \quad y = \pm 1. \tag{6}$$

Among the solutions of the above equations, the simplest are the following streamwise modes without cross-stream velocities, obtained as the homogeneous solutions of (4):

$$(\hat{u}_0, \hat{v}_0, \hat{w}_0) = (\cos(m+\tfrac{1}{2})\pi y, 0, 0), \tag{7}$$

with the eigenvalue $\gamma = \{\beta^2+(m+\frac{1}{2})^2\pi^2\}/R$, or

$$(\hat{u}_0, \hat{v}_0, \hat{w}_0) = (\sin(m+1)\pi y, 0, 0) \tag{8}$$

with $\gamma = \{\beta^2+(m+1)^2\pi^2\}/R$, where $m = 0, 1, 2, \ldots$. Using those streamwise modes, we made several attempts to represent the three-dimensional distortion of the experimental basic flow. The results show that the following combination of the lowest ($m = 0$) symmetric (u_s) and antisymmetric(u_a) modes expresses the observed three-dimensionality well:

$$U = 1-y^2+u_\mathrm{s}+u_\mathrm{a}, \tag{9}$$

$$u_\mathrm{s} = 0.015\cos(\tfrac{1}{2}\pi y)\cos\beta_\mathrm{s}(z-z_\mathrm{s}), \tag{10}$$

$$u_\mathrm{a} = 0.01\sin(\pi y)\cos\beta_\mathrm{a}(z-z_\mathrm{a}), \tag{11}$$

where the spanwise wavelengths $2\pi h/\beta_\mathrm{s}$ and $2\pi h/\beta_\mathrm{a}$ are respectively 23 mm and 30 mm, with $z_\mathrm{s}h = 50$ mm and $z_\mathrm{a}h = 55$ mm. Equation (9) is compared with the experimental basic flow in figure 1.

From (3)–(6), we can calculate the possible distortion modes which have all three velocity and vorticity components. Among those with streamwise vortices, particular attention is focused on two solutions. One is the least damped mode, which has a single streamwise vortex across the depth of the channel. The other is the next least damped mode with a double streamwise vortex across the depth. The dotted lines in figure 6(a, b) show the velocity field of the double-vortex mode, while the broken lines in figure 6(c, d) illustrate that of the single-vortex mode. The solid lines in figure 6(a, c) represent the symmetric ($m = 0$ and 1) and antisymmetric ($m = 0$) streamwise modes without cross-stream velocity. As far as the $\hat{u}_0(y)$-distribution is concerned, the single-vortex mode is indistinguishable from the antisymmetric streamwise mode $m = 0$ (i.e. u_a). Such a close similarity is also seen between the double-vortex mode and the symmetric streamwise mode of $m = 1$. In this connection, the lowest symmetric streamwise mode (i.e. u_s) is exceptional in that it has no such a relation with streamwise vortices.

Let us reconsider the distortion in the present experimental basic flow whose u-velocity is well represented by (9). It can be safely said that the part of the distortion whose $\hat{u}_0(y)$ is represented by u_s has no streamwise vortices at all. However, no such assertion is possible for the distortion represented by u_a because of the possibility that it might be of the single-vortex mode whose $\hat{u}_0(y)$ is indistinguishable from u_a as noted above. Importantly, however, the streamwise vortices of the single-vortex mode are extremely weak, and even if they exist in our basic flow at $R = 5000$, they are almost negligible since v_0 and w_0 are three orders of magnitude smaller than u_0, as can be seen from figure 6(c, d).

The following experimental fact gives further insight into the relative importance

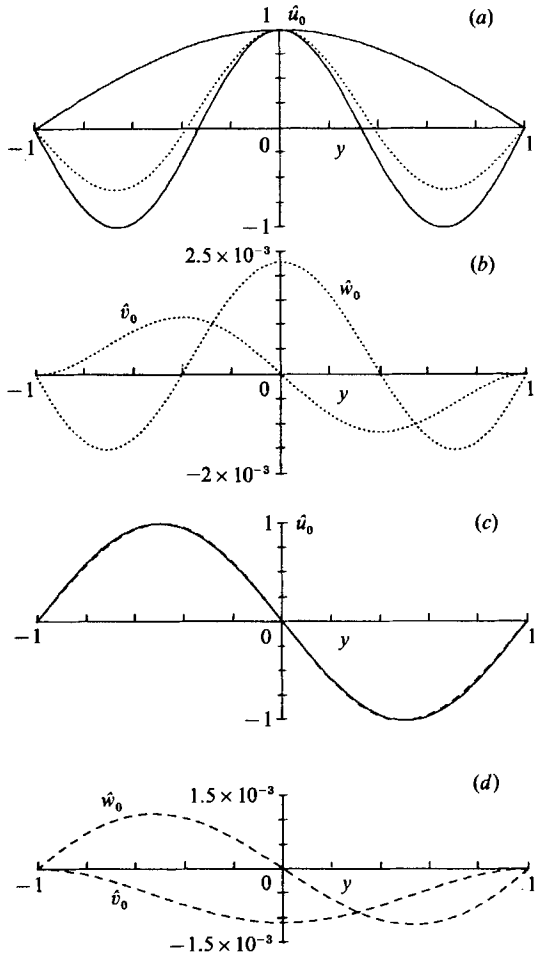

FIGURE 6. Structures of the three-dimensional mean-flow distortion modes at $R = 5000$. Dotted lines in (*a*) and (*b*) are the double-vortex mode ($\beta = 2.0$); broken lines in (*c*) and (*d*) are the single-vortex mode ($\beta = 1.5$). Solid lines in (*a*) and (*c*) represent distortion modes without cross-stream velocities (equation (7) with $m = 0$, 1 and (8) with $m = 0$ respectively).

of these two modes (u_s and u_a) in determining the observed peak–valley structure: the peak states in both halves ($y \gtrless 0$) of the channel always occur at the same z-positions and the spanwise wavelength of the wave motion is determined by the three-dimensional pattern of the centreline velocity. These suggest that the symmetric u_s mode (equation (10)) has a decisive effect on our peak–valley development. This is quite important considering the fact that the u_s mode (which is the least damped among all the distortion modes for given R and β) has no streamwise vorticity.

Through numerical simulations, we shall further investigate the important role of the mean-flow distortion which is directly related to the origin of the three-dimensional wave, and clarify the detailed process leading to the peak–valley structure.

4. Numerical study

4.1. *Formulation of the problem*

We use the incompressible Navier–Stokes equations written in non-dimensional form (scaled with the channel half-depth h and the centreline velocity U_c of the basic parabolic flow),

$$\frac{\partial \boldsymbol{v}}{\partial t}+(\boldsymbol{v}\cdot\boldsymbol{\nabla})\,\boldsymbol{v}=-\boldsymbol{\nabla}p+\frac{1}{R}\nabla^2\boldsymbol{v}, \tag{12}$$

$$\boldsymbol{\nabla}\cdot\boldsymbol{v}=0, \tag{13}$$

where $\boldsymbol{v}(x,y,z,t)=(u,v,w)$ is the velocity field, $p(x,y,z,t)$ the pressure and R the Reynolds number. We assume that the flow develops in time and is periodic in the streamwise (x) and spanwise (z) directions with the dominant wavelengths of $2\pi/\alpha$ and $2\pi/\beta$ respectively, though actually the disturbances evolve in space. The boundary conditions are then written as

$$\boldsymbol{v}=0 \quad \text{at} \quad y=\pm 1, \tag{14}$$

$$\boldsymbol{v}(x+2\pi/\alpha, y, z+2\pi/\beta, t)=\boldsymbol{v}(x,y,z,t). \tag{15}$$

As noted in the introduction, the initial disturbances to be superposed on the basic parabolic flow are given as a linear combination of a two-dimensional T–S mode and a three-dimensional (mean-flow) distortion mode, i.e.

$$\boldsymbol{v}(x,y,z,t=0)=\boldsymbol{U}(y)+A_2\,\boldsymbol{v}_2(x,y,t=0)+A_3\,\boldsymbol{v}_3(y,z,t=0) \tag{16}$$

with

$$\boldsymbol{U}=(1-y^2,0,0), \tag{17}$$

$$\boldsymbol{v}_2=\mathrm{Re}\{\hat{\boldsymbol{v}}_2(y)\,\mathrm{e}^{\mathrm{i}(\alpha x-\omega t)}\}, \tag{18}$$

$$\boldsymbol{v}_3=\tfrac{1}{2}\,\mathrm{Re}\{\hat{\boldsymbol{v}}_3^{+}(y)\,\mathrm{e}^{\mathrm{i}\beta z}+\hat{\boldsymbol{v}}_3^{-}(y)\,\mathrm{e}^{-\mathrm{i}\beta z}\}\,\mathrm{e}^{\gamma t} \tag{19}$$

where $\hat{\boldsymbol{v}}_2$ and $\hat{\boldsymbol{v}}_3^{\pm}$ are the eigensolutions of the linear stability equations. They are normalized respectively such that the maximum amplitude of the streamwise component is unity, so that A_2 and A_3 define the initial amplitudes of the two-dimensional T–S and three-dimensional distortion modes respectively. To simulate our laboratory experiment closely, the Reynolds number R is set at 5000, and the streamwise and spanwise wavenumbers, α and β are selected to be 1.12 and 2.0 respectively: the corresponding eigenvalue $\omega(=\omega_r+\mathrm{i}\omega_i)$ of the two-dimensional T–S wave is 0.3156–0.00279i.

As already discussed in §3, the three-dimensionality in our basic flow can be well represented by the two distortion modes, u_s ($\beta=2.0$) and u_a ($\beta=1.5$) and the experimental evidence further suggests that the symmetric u_s mode is more important for the observed peak–valley development. So, we select the u_s mode ($\beta=2.0$) for the initial mean-flow in the present simulation,

$$(\hat{u}_3^{\pm},\hat{v}_3^{\pm},\hat{w}_3^{\pm})=(\cos(\tfrac{1}{2}\pi y),0,0). \tag{20}$$

The initial mean-flow field is illustrated in figure 7 by comparing it to the approximated experimental basic flow containing the two distortion modes (equation (9) shown in figure 1).

The development of disturbances in time is examined numerically under a constant (mean, streamwise) pressure gradient, $-2/R$, using the Fourier–Chebyshev

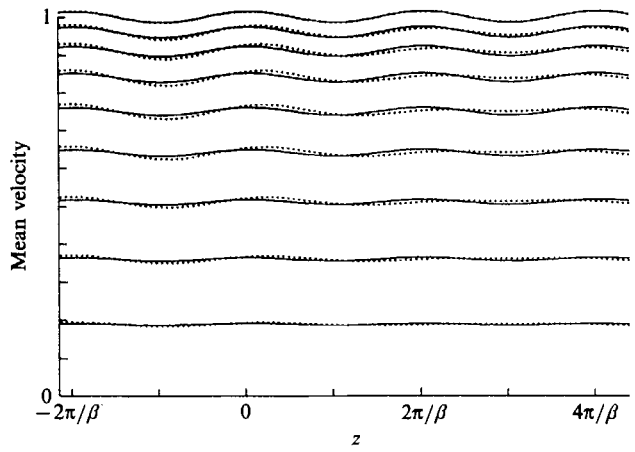

FIGURE 7. Initial mean-flow field: ——, $U+u_s$; ·····, $U+u_s+u_a$ (equation (9)): y (from top) = 0, -0.2, -0.3, -0.4, -0.5, -0.6, -0.7, -0.8, -0.9.

spectral method with a semi-implicit fractional step procedure in time advancement (Orszag & Kells 1980). The velocity is written as follows:

$$\boldsymbol{v}(x,y,z,t) = \sum_{m=0}^{M}\sum_{n=0}^{N} \boldsymbol{v}_{mn}(x,y,z,t), \tag{21}$$

where

$$\boldsymbol{v}_{00}(x,y,z,t=0) = \boldsymbol{U}(y), \tag{22}$$

$$\boldsymbol{v}_{mn} = \mathrm{Re}\{\hat{\boldsymbol{v}}_{m,n}(y,t)\,\mathrm{e}^{\mathrm{i}(m\alpha x+n\beta z)} + \hat{\boldsymbol{v}}_{m,-n}(y,t)\,\mathrm{e}^{\mathrm{i}(m\alpha x-n\beta z)}\} \quad \text{for } n \neq 0, \tag{23}$$

$$\boldsymbol{v}_{m0} = \mathrm{Re}\{\hat{\boldsymbol{v}}_{m,0}(y,t)\,\mathrm{e}^{\mathrm{i}m\alpha x}\}. \tag{24}$$

We take four Fourier modes in the x- as well as the z-directions ($M = N = 3$) and 41 Chebyshev polynomials in the y-direction. As far as the initial stage of the three-dimensional development of interest here is concerned, the resolution ($4\times4\times41$ modes) is sufficient to describe the phenomenon, as shown in the following sections. This is also supported by Kleiser's (1982) numerical solution with $8\times8\times41$ modes. The computation is carried out by using a micro-computer (NEC 9801).

4.2. *Numerical results*

We first describe the results of the simulation for the low-amplitude case of the initial two-dimensional T–S and three-dimensional distortion modes, i.e. $A_2 = 0.6\,\%$ and $A_3 = 0.5\,\%$. Figure 8 illustrates the development of the Fourier modes, $\boldsymbol{v}_{10}$, $\boldsymbol{v}_{01}$ and $\boldsymbol{v}_{11}$, tracing the time evolution of their energies (scaled with that of the basic parabolic flow), E_{mn}:

$$E_{mn} = \frac{15\alpha\beta}{64\pi^2}\int_0^{2\pi/\beta}\mathrm{d}x\int_0^{2\pi/\alpha}\mathrm{d}z\int_{-1}^{1}(\boldsymbol{v}_{mn}\cdot\boldsymbol{v}_{mn})\,\mathrm{d}y. \tag{25}$$

Both the two- and three-dimensional primary modes (E_{10} and E_{01}) indicate an exponential decay with almost the same damping rates as those given by linear stability theory (dotted and broken lines respectively). We have furthermore confirmed that they maintain their initial structures and do not change over time. The three-dimensional wave mode of interest here, $\boldsymbol{v}_{11}$, which is generated by the coupling between the primary modes ($\boldsymbol{v}_{10}$ and $\boldsymbol{v}_{01}$), is extremely weak and also decays exponentially as $\exp(\omega_i+\gamma)t$ after passing the transient period, i.e. for $t > 70$.

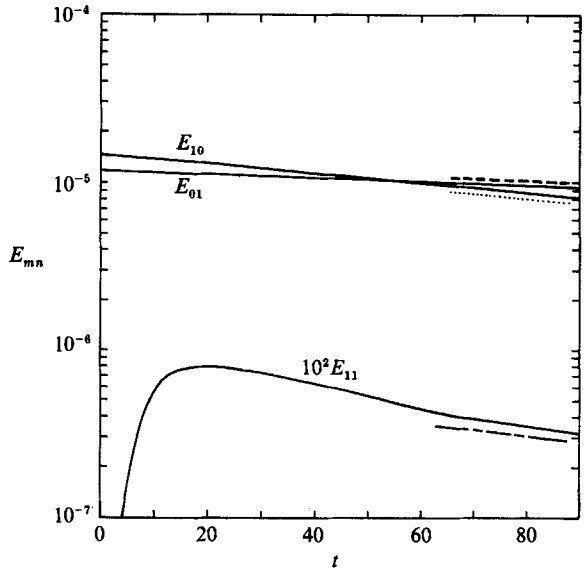

FIGURE 8. Time evolution of E_{mn} with initial conditions $A_2 = 0.6\%$ and $A_3 = 0.5\%$. ·····, $\exp(2\omega_i t)$; – – –, $\exp(2\gamma t)$; —·—, $\exp(2(\omega_i+\gamma)t)$.

Maintaining A_2 at 0.6%, we increased the magnitude of the initial three-dimensional distortion mode (A_3) to 5% to see the dependency of the disturbance development on the magnitude of the initial three-dimensionality contained in the basic flow, but we could not find any noticeable change in the structure and behaviour of the two- and three-dimensional modes except that v_{11} increases in proportion to A_3; namely, when the two-dimensional T–S wave is weak, the three-dimensional wave v_{11} is simply generated by the second-order coupling between v_{10} and v_{01} and nothing more interesting occurs, at least in the range of A_3 examined. To more fully examine the structure of v_{11} thus generated for the case of the weak two-dimensional T–S wave, we also solved linear non-homogeneous equations for v_{11} taking into account only the nonlinear coupling between the primary v_{10} and v_{01} modes. The result will be described in §4.3.

On the other hand, the intensity of the two-dimensional T–S mode has a crucial effect on the development of the three-dimensional wave mode. Figure 9 compares different features of the development of the three-dimensional mode v_{11} for various magnitudes of the initial two-dimensional mode A_2 (from 0.6 to 3.0%) with a fixed A_3 of 0.5%, by plotting its energy scaled with the magnitude of the primary modes, i.e. $E_{11}(t)/(A_2A_3)^2$. In each case, there is little doubt that the three-dimensional wave mode is generated first in the same way as in the low-amplitude case ($A_2 = 0.6\%$). However, for A_2 beyond 1%, the final evolution deviates from the second-order behaviour (characterized as $\exp(\omega_i+\gamma)t$), that is, the three-dimensional wave mode starts to grow. This suggests that 'additional interactions' come to play beyond the threshold for A_2, as explained below. If the nonlinear effects are merely governed by the second-order coupling between the primary modes (v_{10} and v_{01}) as is the case below the threshold, the streamwise and spanwise stretching of vorticity cannot operate because of the absence of the streamwise vorticity, and then the three-dimensional wave is generated mainly by the tilting of the spanwise vorticity. In this regard, we are interested in the change in the structure of the three-dimensional

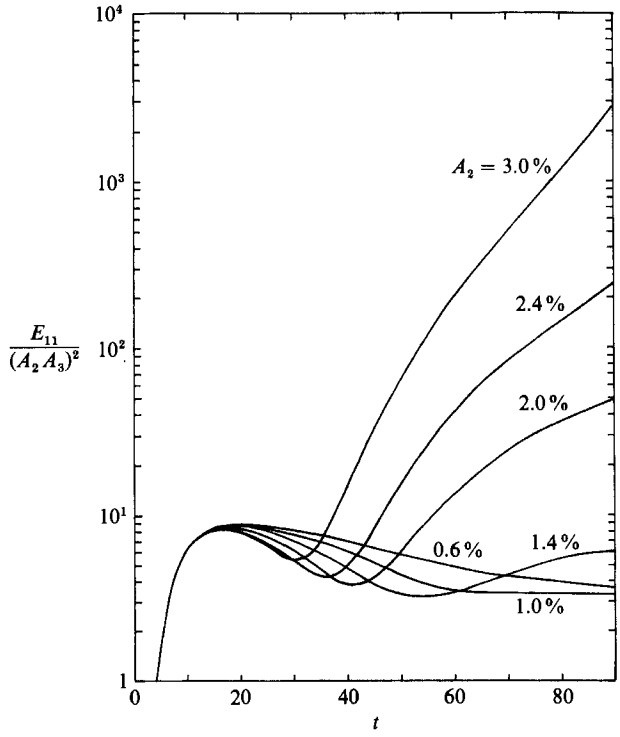

FIGURE 9. Energy of the three-dimensional mode E_{11} *vs.* time for various initial amplitudes A_2 from 0.6% to 3.0%, with a fixed value of A_3 of 0.5%.

distortion mode ($\boldsymbol{v}_{01}$) for the growth cases $A_2 = 2.0$, 2.4 and 3.0%. Figure 10 compares the y-distributions of the three components of $\boldsymbol{v}_{01}$ observed at $t = 90$ for $A_2 = 0.6$, 2.0, 2.4 and 3.0%. We notice that the three-dimensional distortion mode ($\boldsymbol{v}_{01}$) changes its structure at and around the critical layer, and more importantly the cross-stream velocity components (and therefore the streamwise vorticity develops as the magnitude of the two-dimensional T–S mode (A_2) increases. The new generation of the streamwise vorticity (or vortex) may cause the three-dimensional wave mode to grow through the effects of vortex stretching as well as tilting which together with the convection effect work on the main spanwise vorticity and are definitely responsible for the three-dimensional growth as Orszag & Patera (1983) point out. Therefore the 'additional interactions' should be such that they can generate $\boldsymbol{v}_{01}$ with the cross-stream velocity components, i.e. the streamwise vortices: the most important among the possible 'additional interactions' is no doubt that between the two-dimensional T–S mode ($\boldsymbol{v}_{10}$) and the newly generated $\boldsymbol{v}_{11}$.

In such growth cases the three-dimensional wave mode develops almost exponentially as if it were caused by a certain linear instability. This is probably because the magnitude of $\boldsymbol{v}_{10}$ is maintained nearly constant over time. Here, the largest value of the initial two-dimensional amplitude ($A_2 = 3.0\%$) is almost equal to the two-dimensional equilibrium amplitude calculated by Herbert (1977), so comparison of the disturbance development in this case to the secondary instability model is of interest. Figure 11 traces the evolution of the two-dimensional T–S mode and various three-dimensional modes of the same spanwise wavenumber β, in terms of E_{10} and E_{m1} ($m = 0$, 1, 2). The result indicates that the three-dimensional modes

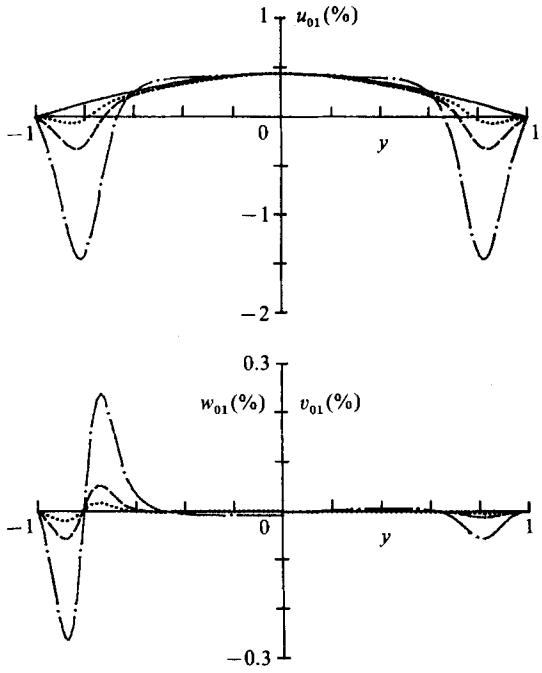

FIGURE 10. y-distributions of u_{01}, v_{01} and w_{01} at $t = 90$, for the initial value $A_2 = 0.6\%$ (——), 2.0% (·····), 2.4% (– – –) and 3.0% (—·—); A_3 is fixed at 0.5%. Note that the distributions of v_{01} (antisymmetric in y) and w_{01} (symmetric in y) are respectively given in the positive- and negative-y region only.

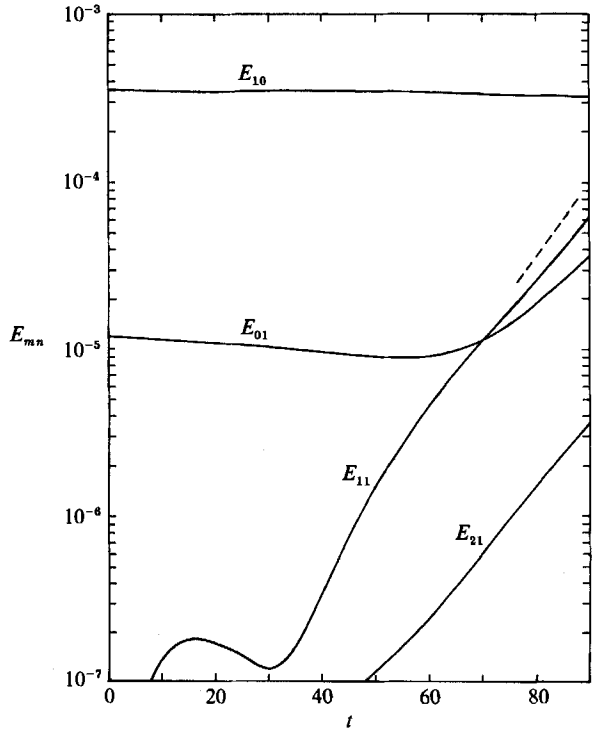

FIGURE 11. Time evolution of E_{mn} with initial conditions $A_2 = 3.0\%$ and $A_3 = 0.5\%$. The broken line indicates the growth rate from Herbert's model (1984*b*).

all grow almost exponentially with the same exponent (for the three-dimensional distortion mode E_{01}, this is the case for $t > 80$), while the two-dimensional mode maintains an equilibrium state for the whole calculation time. It is also noted that the three-dimensional modes of spanwise wavenumber 2β (such as $\boldsymbol{v}_{02}$ and $\boldsymbol{v}_{12}$) are weak compared with the $\boldsymbol{v}_{11}$ mode up to the stage shown here, though they are growing with an exponent twice that of the $\boldsymbol{v}_{11}$ mode. Herbert (1984*a*, *b*) interpreted this feature to mean that the streamwise periodic flow caused by the two-dimensional T–S wave of the equilibrium (or near-equilibrium) amplitude is unstable with respect to three-dimensional disturbances. Applying the Floquet theory to the linearized equations for three-dimensional disturbances, he obtained a three-dimensional eigenmode of the form

$$\boldsymbol{v} = \mathrm{e}^{\sigma t} \sum_{n=\pm 1} \mathrm{e}^{\mathrm{i}n\beta z} \sum_{m=-\infty}^{+\infty} \hat{\boldsymbol{v}}_{mn}(y)\, \mathrm{e}^{\mathrm{i}m\alpha(x-ct)}, \tag{26}$$

where σ is the growth rate which he calculated to be 0.0509 for the case of the same flow parameters (R, α, β and A_2) as the present. His growth curve, represented by the broken line in the figure, shows good agreement with the present simulation. Thus we expect that the structural change in the three-dimensional mean-flow distortion mode (and the occurrence of streamwise vortices) can be interpreted by using Herbert's secondary instability model. So figure 12 compares the y-distributions of the u_{01}, v_{01} and w_{01} components for the case $A_2 = 3.0\,\%$ (at $t = 90$) with the corresponding ones of Herbert's model where, for u_{01}, the initial three-dimensional distortion mode is superposed on the eigenmode. The magnitude of the eigenmode is chosen so that the maximum amplitude of u_{11} (streamwise velocity component of the three-dimensional wave) coincides with that of the simulation. We find a close similarity between the structures of the present calculation and Herbert's model. Furthermore, we have examined the behaviour of various three-dimensional modes in the other two cases of lower amplitudes $A_2 = 2.0$ and $2.4\,\%$, and found that the second-harmonic three-dimensional wave mode ($\boldsymbol{v}_{21}$) and the cross-stream components of the mean-flow distortion (v_{01} and w_{01}) also develop with almost the same exponent as that of the $\boldsymbol{v}_{11}$ mode, though the exponent is of course smaller than that for the case $A_2 = 3.0\,\%$ as seen in figure 9.

As for the initial three-dimensional disturbances, the present numerical simulation demonstrates that the mean-flow distortion alone can cause the subcritical three-dimensional instability leading to the peak–valley structure, provided that A_2 is above the threshold. In this case, as we have seen in figure 10, the change in the structure of the mean-flow three-dimensionality occurs only near the walls as if the newly generated three-dimensional distortion mode were superposed on the initial mean-flow distortion. That is, once the initial three-dimensionality generates the three-dimensional wave disturbance through the interaction with the two-dimensional T–S wave, the additional interactions between the two- and three-dimensional wave modes operate to generate streamwise vorticity, and the resulting efficient three-dimensional growth seems to be well described by Herbert's model.

4.3. *Comparisons with the experiment*

Let us compare the present numerical results with our laboratory experiments, which are the only experiments available for comparison. We should first examine whether the observed three-dimensionality of the wave really originates from the interaction between the two-dimensional T–S wave and the three-dimensional distortion mode, as demonstrated by the simulation. Figure 13 compares the actual y-distributions of amplitude and phase of u_{11} (the dominant three-dimensional mode) in the case of

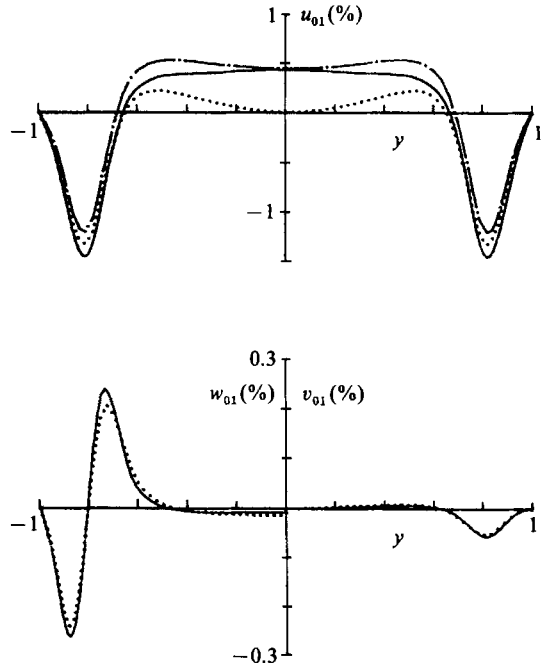

FIGURE 12. Comparison for the three-dimensional distortion mode v_{01} between the present simulation and Herbert's secondary instability model: ——, simulation ($A_2 = 3.0\,\%$, $t = 90$); ·····, Herbert's eigenmode; —·—, Herbert's eigenmode plus the present initial three-dimensional distortion mode ($\cos(\frac{1}{2}\pi y)$, 0, 0).

weak excitation (given in figure 2) with the corresponding results of the simulation (solid lines) and also with those calculated (as mentioned earlier) from the disturbance equations for v_{11} taking into account only the coupling between the primary v_{10} and v_{01} modes (broken lines). In figure 13 (*b*), the phase distribution of the two-dimensional T–S mode (u_{10}) is added to see the relative phase between the two-dimensional T–S and three-dimensional modes. As a matter of course, the three-dimensional wave mode (v_{11}) resulting from the interaction between the primary two- and three-dimensional modes (v_{10} and v_{01}) is locked in phase to the two-dimensional T–S wave (v_{10}). These comparisons show that the experimentally observed structure of the three-dimensional component is almost the same as that of the simulation and of the calculation taking into account only the second-order coupling between the primary two-dimensional T–S wave and the three-dimensional distortion mode. This is also the case for the phase relationship with the two-dimensional T–S wave. Furthermore, measurements have already indicated that the three-dimensional wave maintains a linear relationship, in magnitude, with the two-dimensional T–S wave when the latter is weak (less than about 1 % of U_c); see figure 5. All these features no doubt result from the second-order coupling as already concluded from the results of the simulation. The reason why we have thus far been so careful in concluding this feature must be explained, namely, there is a possibility that the ribbon vibrating in the three-dimensional basic flow may directly generate three-dimensional wave disturbances together with the two-dimensional T–S wave. Even if it is the case, the directly ribbon-induced three-dimensional wave may decay downstream according to linear stability theory, with a large damping rate because the Reynolds number is subcritical. Therefore, even if existed, it would be extremely weak at the

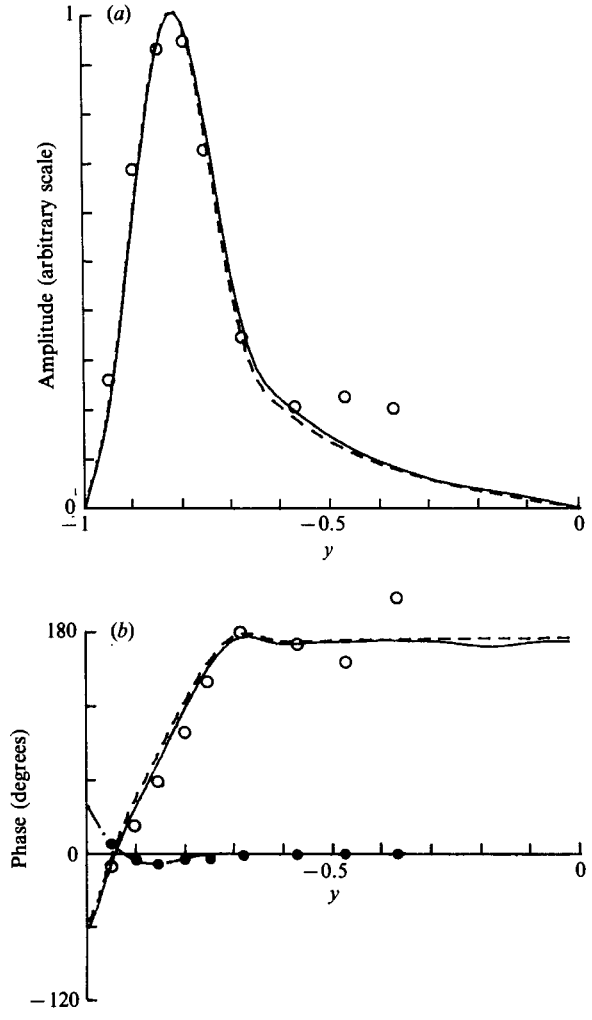

FIGURE 13. Comparisons of (*a*) amplitude and (*b*) phase distributions of the three-dimensional wave mode u_{11} (antisymmetric in y) between experiment at $u'_m/U_c = 0.35\%$ (○), the simulation with initial conditions $A_2 = 0.6\%$ and $A_3 = 0.5\%$, $t = 90$ (——), and calculation taking into account only second-order coupling between primary v_{10} and v_{01} (– – – –). The phase of the two-dimensional wave mode u_{10} (antisymmetric in y) is also plotted: ●, experiment; ——, simulation and distribution of two-dimensional T–S mode.

observation position ($48h$ downstream of the ribbon) unless the intensity were extremely large at the ribbon. This inference is firmly supported by the comparisons in figure 13. So we can say that the observed three-dimensional wave component mainly results from the two and three-dimensional interaction of interest here when the amplitude of the primary T–S wave introduced is not particularly large.

As the magnitude of the primary T–S wave is increased beyond the threshold of about $A_2 = 1.4\%$, the three-dimensional wave component in both the laboratory and numerical experiments begins to grow, leading to the peak–valley wave motion. Figure 14 plots the maximum r.m.s. amplitude of u-fluctuations at $z = 0$, $\pi/2\beta$ and π/β versus time for the three cases $A_2 = 2.0$, 2.4 and 3.0%: The centreline velocity (U_c) takes a local maximum and a local minimum at $z = 0$ and π/β respectively. As

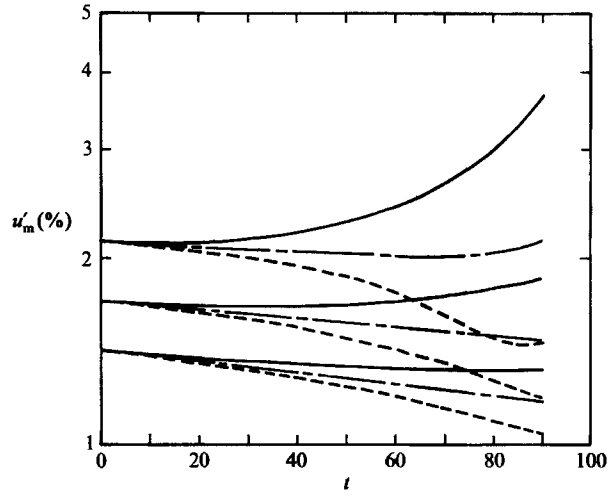

FIGURE 14. Development of u-fluctuation at $z = 0$ (——), $\pi/2\beta$ (– – –) and π/β (– – – –) for the three cases $A_2 = 2.0$, 2.4 and 3.0% with a fixed A_3 of 0.5%. Note that the centreline velocity in the initial flow field takes a local maximum at $z = 0$ and a local minimum at $z = \pi/\beta$; see figure 7.

seen in the figure, the spanwise peak where the wave amplitude is enhanced develops at the z-position of local U_c maximum ($z = 0$) with the valley at the local U_c minimum ($z = \pi/\beta$), in complete agreement with our laboratory experiment, namely, the peak–valley situation is completely determined by the spanwise distortion of the basic flow. Here it should be noted that we observe two-dimensional wave behaviour at the spanwise mid-position ($z = \pi/2\beta$) since the three-dimensional mode of higher spanwise wavenumbers (e.g. the v_{12} mode) is negligible in magnitude.

Another important aspect is the structure of the growing three-dimensional wave mode. So, figure 15 compares the y-distributions of the amplitude and phase of u_{11} (at $t = 90$ for the cases $A_2 = 2.4\%$ and 3%) with those of the laboratory experiment (at the $u'_m/U_c = 1.8\%$ stage). In figure 15(b), the phase distribution of the two-dimensional T–S mode (u_{10}) is also plotted in the same way as in figure 13(b). It was found that in these growth cases too, the three-dimensional wave is locked in phase with the two-dimensional wave. As has already been shown in Nishioka & Asai (1985b), figure 15 confirms that the structure of the eigenmode of the secondary instability model is very close to that of the growing three-dimensional mode in the experiment. Nevertheless, we should point out a slight but non-negligible difference between Herbert's eigenmode and the simulated three-dimensional mode which agrees more closely with the actual three-dimensional wave mode as far as the phase distribution is concerned. This also suggests that the initial three-dimensional disturbance of the present study, i.e. the spanwise distortion of the basic flow (symmetric mode, (10)) really dominates the observed three-dimensional wave development.

In §3, we saw that our experimental basic flow also contains the antisymmetric distortion mode (equation (11)). Although the above results suggest that the antisymmetric mode has no significant effect on the observed three-dimensional wave development, we have to be very careful to conclude this: our experiment will be reproduced more accurately through similar computations which include the antisymmetric distortion mode as the initial condition. The content of the weak antisymmetric distortion mode will distort the y-symmetry of the peak–valley

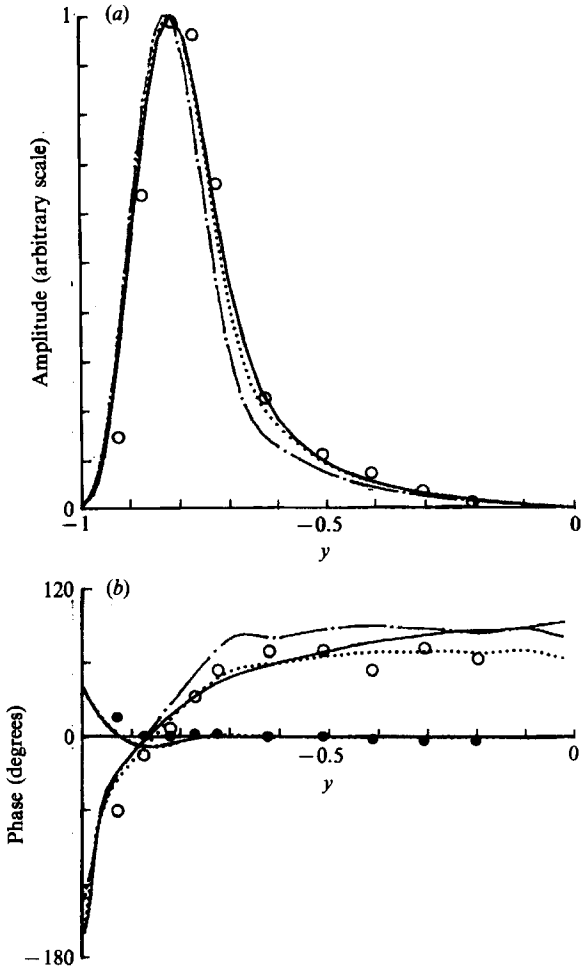

FIGURE 15. Comparisons of (*a*) amplitude and (*b*) phase distributions of the growing three-dimensional wave mode u_{11} between experiment, numerical simulation and Herbert's secondary instability model. ○, experiment ($u'_m/U_c = 1.8\%$) ——, simulation ($t = 90$) for $A_2 = 2.4\%$ and $A_3 = 0.5\%$; ·····, simulation ($t = 90$) for $A_2 = 3.0\%$ and $A_3 = 0.5\%$; ——, Herbert's model. For the phase of the two-dimensional mode, all the corresponding results are shown, as can be seen from the experimental points indicated by ●.

structure slightly because it may excite a symmetric three-dimensional wave through the interaction with the (antisymmetric) two-dimensional T–S wave. Without carrying out such detailed calculations, however, it can be concluded from the present study that through interacting with the two-dimensional T–S wave, the mean-flow distortion can excite the three-dimensional wave leading to the peak–valley development.

5. Concluding remarks

In this paper, we have examined numerically the three-dimensional evolution of the T–S wave in a slightly three-dimensional plane Poiseuille flow at a subcritical Reynolds number $R = 5000$ in detail to understand the process leading to the peak–valley structure observed in our laboratory experiment.

The most important result obtained is that the spanwise distortion of the basic flow causes the peak–valley wave motion to develop through the interaction with the two-dimensional T–S wave when the amplitude of the T–S wave exceeds about 1%, as observed in our laboratory experiments. When the two-dimensional T–S wave is weak, the three-dimensional wave disturbance is generated simply through the weak interaction (the second-order coupling) between the two-dimensional T–S wave and the three-dimensional distortion mode (initially contained in the basic flow), and decays owing to viscous effects as does the two-dimensional T–S wave under the subcritical condition. On the other hand, above the threshold, the disturbance development has the nature of a secondary instability, accompanying the simultaneous growth of longitudinal vortices. In this case, the peak–valley positions are determined by the three-dimensionality of the basic flow just as in our laboratory experiment. Comparisons of the structure of the three-dimensional wave mode between the present simulation and our laboratory experiment clearly show that the three-dimensional evolution numerically observed here really occurs in our plane Poiseuille flow containing slight three-dimensionality in the basic flow.

Nishioka *et al.* (1975) first showed experimentally the occurrence of the subcritical instability in plane Poiseuille flow and obtained qualitative agreement, on the threshold behaviour, between observations and Itoh's (1974) calculation based on the two-dimensional weakly nonlinear theory of Stuart (1960). On the basis of the present numerical study, there is no doubt that in Nishioka *et al.*'s (1975) experiment too, the three-dimensional wave mode was generated, growing when the amplitude of the two-dimensional wave was above the three-dimensional threshold. However, the three-dimensionality of the basic flow (at $R = 5000$) in the 1975 experiment was much weaker than those shown in figure 1, namely the three-dimensional disturbance source was considerably weaker. Furthermore, according to the present study, the z-position where the measurement was taken is judged to be near the mid-position between the spanwise peak and valley because it was located between those of local U_c maximum and minimum. At exactly the mid-position, we observe the behaviour of the two-dimensional wave only. So it appears quite natural that their experimental results demonstrated almost the same behaviour as predicted by weakly nonlinear stability theory for the two-dimensional wave, so long as the three-dimensional wave mode remained weak even though it was growing.

Finally, from the present study, it can be concluded that the process leading to the peak–valley structure initially caused by the spanwise distortion in the basic flow can occur in Blasius flow too, just as in plane Poiseuille flow. Indeed, in Klebanoff *et al.*'s (1959, 1962) experiment too, the weak spanwise distortion of the basic flow is no doubt responsible for the peak–valley wave growth.

The authors wish to express their sincere gratitude to Professors S. Iida, I. Tani and H. Sato for their continual encouragement and to Mr K. Suzuki for his enthusiastic help in carrying out the experiment and the data analyses.

REFERENCES

BENNEY, D. J. & LIN, C. C. 1960 On the secondary motion induced by oscillations in a shear flow. *Phys. Fluids* **3**, 656–657.

CRAIK, A. D. D. 1971 Nonlinear resonant instability in boundary layers. *J. Fluid Mech.* **50**, 393–413.

CRAIK, A. D. D. 1985 *Wave Interactions and Fluid Flows*. Cambridge Monographs on Mech. and Applied Math. Cambridge University Press.

DHANAK, M. R. 1983 On certain aspects of three-dimensional instability of parallel flows. *Proc. R. Soc. Lond.* A **385**, 53–84.

DIPRIMA, R. C. & HABETLER, G. J. 1969 A completeness theorem for non-selfadjoint eigenvalue problems in hydrodynamic stability. *Arch. Rat. Mech. Anal.* **34**, 218–227.

FASEL, H. & BESTEK, H. 1980 Investigation of nonlinear, spatial disturbance amplification in plane Poiseuille flow. In *Laminar–Turbulent Transition* (ed. R. Eppler & H. Fasel), pp. 173–185. Springer.

HAMA, F. R. & NUTANT, J. 1963 Detailed flow-field observations in the transition process in a thick boundary layer. In Proc. 1963 Heat Transfer and Fluid Mech. Institute, Stanford University, pp. 77–93.

HERBERT, TH. 1977 Finite amplitude stability of plane parallel flows. *AGARD CP*-224, 3.1–3.10.

HERBERT, TH. 1984*a* Secondary instability of shear flow. *AGARD Rep.* 709.

HERBERT, TH. 1984*b* Modes of secondary instability in plane Poiseuille flow. In *Turbulence and Chaotic Phenomena in Fluids* (ed. T. Tatsumi), pp. 53–58. North-Holland.

HERBERT, TH. & MORKOVIN, M. V. 1980 Dialogue on bridging some gaps in stability and transition research. In *Laminar–Turbulent Transition* (ed. R. Eppler & H. Fasel), pp. 47–72. Springer.

ITOH, N. 1974 Spatial growth of finite wave disturbances in parallel and nearly parallel flows, I. The theoretical analysis and the numerical results for plane Poiseuille flow. *Trans. Japan Soc. Aeron. Space Sci.* **17**, 160–174.

ITOH, N. 1980 Three-dimensional growth of finite wave disturbances in plane Poiseuille flow. *Trans. Japan Soc. Aeron. Space Sci.* **23**, 91–103.

ITOH, N. 1987 Another route to the three-dimensional development of Tollmien–Schlichting waves with finite amplitude. *J. Fluid Mech.* **181**, 1–16.

KACHANOV, YU, S. & LEVCHENKO, V. YA. 1984 The resonant interaction of disturbances at laminar–turbulent transition in a boundary layer. *J. Fluid Mech.* **138**, 209–247.

KLEBANOFF, P. S. & TIDSTROM, K. D. 1959 Evolution of amplified waves leading to transition in a boundary layer with zero pressure gradient. *NASA Tech. Note* D-195.

KLEBANOFF, P. S., TIDSTROM, K. D. & SARGENT, L. M. 1962 The three-dimensional nature of boundary layer instability. *J. Fluid Mech.* **12**, 1–34.

KLEISER, L. 1982 Spectral simulations of laminar–turbulent transition in plane Poiseuille flow and comparison with experiments. *Lecture Notes in Physics*, vol. 170, pp. 280–285. Springer.

KOVASZNAY, L. S. G., KOMODA, H. & VASUDEVA, B. R. 1962 Detailed flow field in transition. In *Proc. 1962 Heat Transfer and Fluid Mech. Institute, Stanford University*, pp. 1–26.

KOZLOV, V. V. & RAMAZANOV, M. P. 1983 Development of finite amplitude disturbances in a Poiseuille flow. *Izv. Akad. Nauk SSSR, Mekh. Zhid. i Gaza* 43–47.

MORKOVIN, M. V. 1983 Understanding transition to turbulence in shear layers. *Dept Mech. Aerosp. Engng, Illinois Inst. Tech., Chicago, Rep.* AFOSR-FR-83.

NISHIOKA, M. & ASAI, M. 1984 Evolution of Tollmien–Schlichting waves into wall turbulence. In *Turbulence and Chaotic Phenomena in Fluids* (ed. T. Tatsumi), pp. 87–92. North-Holland.

NISHIOKA, M. & ASAI, M. 1985*a* Some observations of subcritical transition in plane Poiseuille flow. *J. Fluid Mech.* **150**, 441–450.

NISHIOKA, M. & ASAI, M. 1985*b* Three-dimensional wave-disturbances in plane Poiseuille flow. In *Laminar–Turbulent Transition* (ed. V. V. Kozlov), pp. 173–182. Springer.

NISHIOKA, M., ASAI, M. & IIDA, S. 1980 An experimental investigation of the secondary instability. In *Laminar–Turbulent Transition* (ed. R. Eppler & H. Fasel), pp. 37–46. Springer.

NISHIOKA, M., ASAI, M. & IIDA, S. 1981 Wall phenomena in the final stage of transition to turbulence. In *Transition and Turbulence* (ed. R. E. Meyer), pp. 113–126. Academic.

NISHIOKA, M., IIDA, S. & ICHIKAWA, Y. 1975 An experimental investigation of the stability of plane Poiseuille flow. *J. Fluid Mech.* **72**, 731–751.

NISHIOKA, M., IIDA, S. & KANBAYASHI, S. 1978 An experimental investigation of the subcritical instability in plane Poiseuille flow. In *Proc. 10th Turbulence Symposium, Inst. Space Aeron. Sci., Tokyo University*, pp. 55–62.

ORSZAG, S. A. & KELLS, L. C. 1980 Transition to turbulence in plane Poiseuille flow and plane Couette flow. *J. Fluid Mech.* **96**, 159–205.

ORSZAG, S. A. & PATERA, A. T. 1983 Secondary instability of wall-bounded shear flows. *J. Fluid Mech.* **128**, 347–385.

SARIC, W. S. & THOMAS, A. S. W. 1984 Experiments on the subharmonic route to turbulence in boundary layers. In *Turbulence and Chaotic Phenomena in Fluids* (ed. T. Tatsumi), pp. 117–122. North-Holland.

SINGER, B. A., REED, H. L. & FERZIGER, J. H. 1986 Investigation of the effects of initial disturbances on plane channel transition. *AIAA Paper* 86-0433.

SINGER, B. A., REED, H. L. & FERZIGER, J. H. 1987 Effect of streamwise vortices on transition in plane channel flow. *AIAA Paper* 87-0048.

STUART, J. T. 1960 On the non-linear mechanics of wave disturbances in stable and unstable parallel flows, I. The basic behaviour in plane Poiseuille flow. *J. Fluid Mech.* **9**, 353–370.

STUART, J. T. 1962 On three-dimensional non-linear effects in the stability of parallel flow. *Adv. Aero. Sci.* **3**, 121–142.

STUART, J. T. 1965 The production of intense shear layers by vortex stretching and convection. *AGARD Rep.* 514.

STUART, J. T. 1986 Stewartson memorial lecture: Hydrodynamic stability and turbulent transition. In *Numerical and Physical Aspects of Aerodynamic Flows III*, pp. 23–38. Springer.

TANI, I. 1981 Three-dimensional aspects of boundary-layer transition. *Proc. Indian Acad. Sci.* **4**, 219–238.